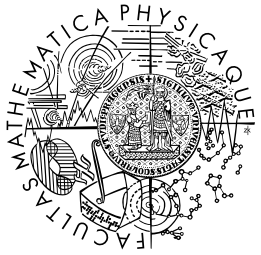

FACULTY
OF MATHEMATICS
AND PHYSICS
Charles University

MASTER THESIS

Dávid Hvizdoš

Two-dimensional model of dissociative recombination

Institute of Theoretical Physics

Supervisor of the master thesis:	RNDr. Karel Houfek, Ph.D.
Study programme:	Physics
Study branch:	Theoretical physics

Prague 2016

I declare that I carried out this master thesis independently, and only with the cited sources, literature and other professional sources.

I understand that my work relates to the rights and obligations under the Act No. 121/2000 Sb., the Copyright Act, as amended, in particular the fact that the Charles University has the right to conclude a license agreement on the use of this work as a school work pursuant to Section 60 subsection 1 of the Copyright Act.

In ..... date ..... signature of the author

Title: Two-dimensional model of dissociative recombination

Author: Dávid Hvizdoš

Institute: Institute of Theoretical Physics

Supervisor: RNDr. Karel Houfek, Ph.D., Institute of Theoretical Physics

Abstract: The purpose of this thesis is to construct a numerically solvable quantum mechanical model describing the dynamics of the indirect mechanism of the dissociative recombination process of a molecular cation by electron impact. The model also describes vibrational excitation of a molecular cation by electron impact. The solution of this model is carried out by implementing a combination of finite elements, discrete variable representation and exterior complex scaling methods. This is then specifically applied to the dissociative recombination and vibrational excitation of H_2^+ by an incoming electron. The results can be used to test the accuracy of approximative methods and the programs expanded to cover the cases of other diatomics.

Keywords: dissociative recombination - vibrational excitation - numerical model - molecular ions - finite elements method - discrete variable representation - exterior complex scaling

I would like to thank my thesis supervisor RNDr. Karel Houfek, Ph.D. for all the help, advice and support he has given me and for having so much time and patience.

I also want to thank his student Mgr. Martin Váňa for all the invaluable programming and technical guidance.

Contents

Introduction

When an ionised gas is neutralized by interaction with electrons we call this process recombination. For atomic ions the process is very slow since energy can only be dispersed by radiation or transfer to another body. Molecular ions can transfer this energy by dissociative break-up into the kinetic energy of the dissociation products. This process is called dissociative recombination (DR) and it is quite complicated so despite being very important for the understanding of molecular plasma dynamics, accurate calculations of DR cross sections still exist only for a few of the simplest cases. A good summary of the history of studying this process along with the description of numerous experimental and theoretical methods can be found in M. Larsson's and A.E. Orel's Dissociative Recombination of Molecular Ions [1]. A more in depth analysis of the most commonly used theoretical methods (such as Multi-Channel Quantum Defect Theory and Time-Dependent Wave Packet methods) is presented in [2] and [3].

In this text we shall be solely focused on the DR process of a positive diatomic molecular ion colliding with an electron. Generally, it can occur through two reaction mechanisms:

$$\begin{aligned} \mathrm{AB}^+ + \mathrm{e} \rightarrow \mathrm{AB}^{**} \rightarrow \mathrm{A} + \mathrm{B} \quad & \text{(direct)}, \\ \mathrm{AB}^+ + \mathrm{e} \rightarrow \mathrm{AB}^{*} \rightarrow \mathrm{AB}^{**} \rightarrow \mathrm{A} + \mathrm{B} \quad & \text{(indirect)}. \end{aligned}$$

In the direct mechanism the incoming electron is captured in a doubly excited dissociative state of the neutral molecule (called a resonant state). The indirect mechanism contains an intermediate step where the electron is captured in a singly excited Rydberg state of the neutral molecule. Both mechanisms are schematically illustrated in Fig. 1.

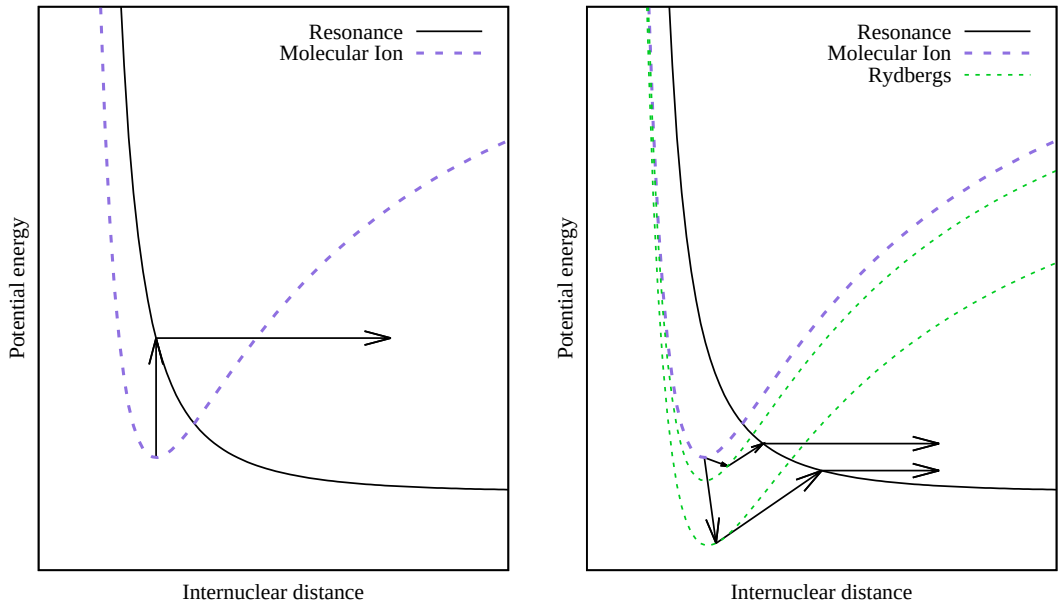

Figure 1: A representation of the direct and indirect DR processes.

The two processes are indistinguishable paths to the same product. They interfere and create sharp peaks in the cross sections as functions of energy.

So far all the theoretical methods used to solve DR have been approximative and also do not differentiate between channels, but provide only the total sum of cross sections. In this thesis we aim to construct a two-dimensional model of DR and solve it numerically without any further approximations. The modeled process is analogous to the indirect mechanism of the DR process (without crossing into the doubly excited resonant state but instead dissociating via low Rydberg states). Within this model we can also obtain the cross sections of vibrational excitation (a much better understood process). Specifically, we will perform our calculations for an $e^-+H_2^+$ system since H_2^+ is the simplest diatomic to model and it is one of the most studied molecular cations (there is a whole chapter devoted to the many experimental and theoretical approaches to the DR process of H_2^+ in [1]). Our results can be then compared to ones gained from the approximative methods.

In the entire thesis we use atomic units

$$m_e = \hbar = e = 4\pi\epsilon_0 = 1.$$

For energy we use Hartrees (1 Ha $\doteq$ 27.211 eV). For distance and cross sections we use the Bohr radius a_0 and squared Bohr radius a_0^2 respectively (1 a_0 $\doteq$ 0.52918 Å).

1. Theory

1.1 Coulomb functions

Before we describe the two dimensional model of dissociative recombination (DR) and vibrational excitation (VE) we start with a discussion of the Coulomb problem which is an important aspect of e^-+AB^+ reactions. If the Hamiltonian of a system consists of a short range potential and the Coulomb potential $-\frac{1}{r}$ the latter one will have a significant impact on the asymptotic forms of the Hamiltonian's eigenfunctions. Let us consider here first a simple Coulomb problem: a single electron affected by a point charge Z (placed in coordinate origin). The Schrödinger equation is then

$$\left(-\frac{\nabla^2}{2} - \frac{Z}{r}\right)\psi_{\vec{k}}(\vec{r}) = \frac{k^2}{2}\psi_{\vec{k}}(\vec{r}), \tag{1.1}$$

where $\vec{k}$ is the particle's asymptotic momentum. The solutions $\psi_{\vec{k}}(\vec{r})$ are called Coulomb wave functions. Expanding these Coulomb wave functions into partial waves we get the sperical Coulomb functions $w_l(\eta,\rho)$ (where $\eta = -Z/k, \rho = kr$) satisfying

$$\frac{\mathrm{d}^2 w_l(\eta,\rho)}{\mathrm{d}\rho^2} + \left(1 - \frac{2\eta}{\rho} - \frac{l(l+1)}{\rho^2}\right) w_l(\eta,\rho) = 0. \tag{1.2}$$

A commonly used basis of two independent solutions are the regular and irregular spherical Coulomb functions $F_l(\eta,\rho)$ and $G_l(\eta,\rho)$ respectively. At $\rho = 0$ F_l behaves like ρ^{l+1} whereas G_l behaves like ρ^{-l}. Their asymptotic behaviour for $\rho \to \infty$ is

$$F_l(\eta,\rho) \xrightarrow[\rho\to\infty]{} \sin\left[\rho - \eta\log(2\rho) - \frac{l\pi}{2} + \arg\Gamma(l+1+i\eta)\right] + O(\rho^{-1}), \tag{1.3}$$

$$G_l(\eta,\rho) \xrightarrow[\rho\to\infty]{} \cos\left[\rho - \eta\log(2\rho) - \frac{l\pi}{2} + \arg\Gamma(l+1+i\eta)\right] + O(\rho^{-1}). \tag{1.4}$$

We sometimes combine them into a new basis $u_l^{\pm} = G_l \pm iF_l$ with exponential asymptotic behaviour

$$u_l^{\pm}(\eta,\rho) \xrightarrow[\rho\to\infty]{} e^{\pm\left[\rho - \eta\log(2\rho) - \frac{l\pi}{2} + \arg\Gamma(l+1+i\eta)\right]} + O(\rho^{-1}). \tag{1.5}$$

1.2 Two dimensional model

The idea is to create a numerically solvable model of electron collisions with molecular cations (with charge $Z = 1$) with an electronic degree of freedom r and a nuclear degree of freedom R. The model Hamiltonian is chosen as

$$H = H_0 + V_{\mathrm{int}}(R,r) = H_0^{\mathrm{ion}} + H_0^{\mathrm{el}} + V_{\mathrm{int}}(R,r), \tag{1.6}$$

where the first term is the Hamiltonian describing the vibrational motion of a molecular cation

$$H_0^{\mathrm{ion}} = -\frac{1}{2\mu}\frac{\partial^2}{\partial R^2} + V_0(R), \tag{1.7}$$

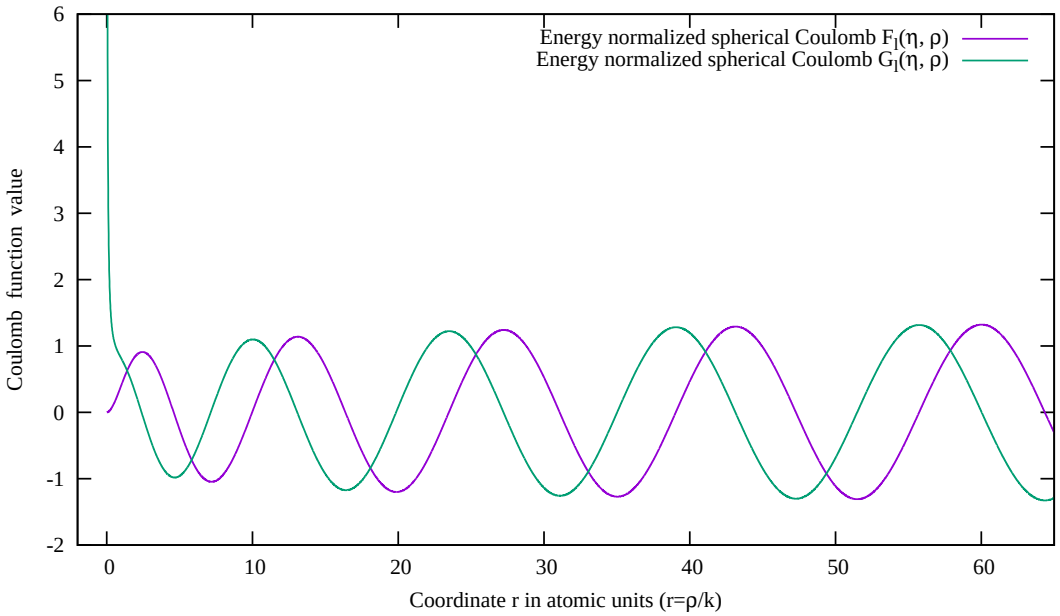

Figure 1.1: An example of energy normalized (multiplied by $\sqrt{\frac{2}{\pi k}}$) spherical Coulomb functions F and G with parameters: $E = 0.05$ Hartree, $k = \sqrt{2E}$, $\eta = -Z/k = -1/k$ and angular momentum $l = 1$.

in which the first term is the nuclear kinetic energy operator (μ is the reduced mass of the molecular cation) and $V_0(R)$ is the potential which describes the vibrational motion of the molecular cation. The second term of the full Hamiltonian is

$$H_0^{\text{el}} = -\frac{1}{2}\frac{\partial^2}{\partial r^2} - \frac{1}{r} + \frac{l(l+1)}{2r^2}, \tag{1.8}$$

where the first term is the electronic kinetic energy operator followed by a Coulombic and a centrifugal term. It describes the incoming electron with angular momentum l attracted by the long range Coulomb field of the molecular ion. The third term of H is the interaction potential coupling the nuclear and electronic degree of freedom

$$V_{\text{int}}(R, r) = -\lambda_1(R)\frac{e^{-\lambda_2(R)r^2}}{r}, \tag{1.9}$$

where the functions $\lambda_1(R)$ and $\lambda_2(R)$ determine the molecule-electron interaction. They control the depth (λ_1) and width (λ_2) of a potential well. If we combine all the non-kinetic terms into one potential

$$V(R, r) = V_0(R) - \frac{1}{r} + \frac{l(l+1)}{2r^2} + V_{int}(R, r), \tag{1.10}$$

we see, that the sole term that remains as $r \to \infty$ is $V_0(R)$. On the other hand, $V_{\text{int}}(R, r)$ does not generally vanish for large internuclear distances and we define

$$V_{\text{int}}^{\infty}(r) = \lim_{R\to\infty} V_{\text{int}}(R, r). \tag{1.11}$$

As we mentioned earlier, we are interested in the vibrational excitation and dissociative recombination processes. The wave function $\psi_E^+(R, r)$ of the whole system satisfies the Schrödinger equation

$$H\psi_E^+(R, r) = E\psi_E^+(R, r). \tag{1.12}$$

This combined with boundary conditions can be rewritten into the Lippmann-Schwinger equation of the form

$$\left|\psi_E^+\right\rangle = |\psi_{in}\rangle + G^+(E)V_{\text{int}}\,|\psi_{in}\rangle = |\psi_{in}\rangle + |\psi_{sc}\rangle\,, \tag{1.13}$$

where $G^+(E) = \lim_{\varepsilon\to 0^+}(E - H + i\varepsilon)^{-1}$ is the appropriate Green's function, $|\psi_{in}\rangle$ is the eigenfunction of H_0 (the non-interacting part of the Hamiltonian) and we defined the scattered part of the wave function $G^+(E)V_{\text{int}}\,|\psi_{in}\rangle = |\psi_{sc}\rangle$. As eigenfunctions of H and H_0, $\left|\psi_E^+\right\rangle$ and $|\psi_{in}\rangle$ now follow the relations

$$(E - H)\left|\psi_E^+\right\rangle = 0, \tag{1.14}$$

$$(E - H_0)\,|\psi_{in}\rangle = 0. \tag{1.15}$$

Now, since we wish to study DR and VE, we set the initial state $\psi_{in}(R, r)$ as follows

$$\psi_{in}(R, r) = \chi_{v_i}(R)\phi_{k_i,l}(r), \tag{1.16}$$

where $\phi_{k_i,l}(r)$ is the wave function of an incoming electron with momentum k_i and angular momentum l. Thus it is an eigenstate of (1.8) so

$$H_0^{\text{el}}\phi_{k_i,l}(r) = \frac{k_i^2}{2}\phi_{k_i,l}(r). \tag{1.17}$$

It is related to an energy normalized Coulomb wave function

$$\phi_{k_i,l}(r) = \sqrt{\frac{2}{\pi k_i}}F_l\left(-\frac{1}{k_i}, k_i r\right). \tag{1.18}$$

The nuclear coordinate function $\chi_{v_i}(R)$ is the initial molecular vibrational state which is a bound eigenstate of (1.11)

$$H_0^{\text{ion}}\chi_{v_i}(R) = E_{v_i}\chi_{v_i}(R), \tag{1.19}$$

and the total energy from (1.12) is

$$E = E_{v_i} + \frac{k_i^2}{2}. \tag{1.20}$$

The boundary conditions for the scattered wave are

$$\psi_{sc}(R, r) \xrightarrow[r\to\infty]{} \sqrt{\frac{2}{\pi k_i}}\sum_{v_f} f^{\text{VE}}_{v_i\to v_f}\chi_{v_f}(R)u_l^+(k_{ef}r), \tag{1.21}$$

$$\psi_{sc}(R, r) \xrightarrow[R\to\infty]{} \sqrt{\frac{2}{\pi k_i}}\sum_{n} f^{\text{DR}}_{v_i\to n}\rho_n(r)K_nRh_l^+(K_nR), \tag{1.22}$$

where $u_l^+(k_{ef}r)$ is the combined Coulomb function with exponential asymptotic behaviour and $h_l^+(K_nR)$ is an outgoing spherical Hankel function. The scattering amplitudes $f^{\text{VE}}_{v_i\to v_f}$ and $f^{\text{DR}}_{v_i\to n}$ are closely related to the so called T matrix which will be defined below. In (1.21) the sum runs over all open vibrational excitation channels. So the function $\chi_{v_f}(R)$ is the final vibrational state with energy E_{v_f} and k_{e_f} is the corresponding momentum of the electron. Their relation to the

total energy is like that in Eq. (1.20). In (1.22) the function $\rho_n(r)$ is a Rydberg state function of the electron satisfying

$$[H_0^{\rm el} + V_{\rm int}^{\infty}(r)]\rho_n(r) = E_n\rho_n(r), \tag{1.23}$$

and again the energy E_n and momentum K_n are connected to the total energy in a relation analogous to (1.20)

$$E = E_{\rm n} + \frac{K_n^2}{2\mu}. \tag{1.24}$$

With a given $\psi_{in}(R,r)$ and total energy we can find the desired wave function $\left|\psi_E^+\right\rangle$ from (1.13). Afterwards we can calculate the T-matrices for dissociative recombination and vibrational excitation as

$$T^{\rm VE}_{v_i\to v_f}(E) = \left\langle \chi_{v_f}\phi_{k_f,l}\right| V_{\rm int}\left|\psi_E^+\right\rangle = \sqrt{\frac{k_i}{k_{ef}}}\frac{f^{\rm VE}_{v_i\to v_f}}{\pi}, \tag{1.25}$$

$$T^{\rm DR}_{v_i\to n}(E) = \left\langle \psi_n^{DR}\right| V_{\rm DR}\left|\psi_E^+\right\rangle = \sqrt{\frac{k_i}{\mu K_n}}\frac{f^{\rm DR}_{v_i\to n}}{\pi}, \tag{1.26}$$

with the DR channel potential

$$V_{\rm DR}(R,r) = V_{\rm int}(R,r) - V_{\rm int}^{\infty}(r) + V_0(R). \tag{1.27}$$

The outgoing states for vibrational excitation are of the same form as the initial state. For dissociative recombination the outgoing states are a product of an unperturbed molecular continuum state with momentum K_n and zero angular momentum and a bound n-th Rydberg state of the electron $\rho_n(r)$ with energy E_n

$$\psi_n^{DR}(R,r) = \sqrt{\frac{2\mu}{\pi K_n}}\sin(K_nR)\rho_n(r), \tag{1.28}$$

They are energy-normalized solutions to the Schrödinger equation with the Hamiltonian

$$H_0^{\rm DR} = -\frac{1}{2}\frac{\partial^2}{\partial r^2} - \frac{1}{2\mu}\frac{\partial^2}{\partial R^2} - \frac{1}{r} + \frac{l(l+1)}{2r^2} + V_{\rm int}^{\infty}(r), \tag{1.29}$$

which is the large internuclear distance limit of the original full Hamiltonian. Finally, the cross sections are

$$\sigma^{\rm VE}_{v_i\to v_f}(E) = \frac{4\pi^3}{k_i^2}\left|T^{\rm VE}_{v_i\to v_f}(E)\right|^2, \tag{1.30}$$

$$\sigma^{\rm DR}_{v_i\to v_f}(E) = \frac{4\pi^3}{k_i^2}\left|T^{\rm DR}_{v_i\to v_f}(E)\right|^2. \tag{1.31}$$

1.2.1 Model for e^-+H_2^+

The potential energy curve of H_2^+ is well approximated by the Morse potential, so for V_0 we use

$$V_0(R) = \beta_1 \left(e^{-2\beta_2(R-R_0)} - 2e^{-\beta_2(R-R_0)}\right), \tag{1.32}$$

where the parameters β_1, β_2 are fitted to closely approximate the lowest electronic state of the molecular cation (their values for the $^1\Sigma_g^+$ state of H_2^+ are in Table 1.1). For the potential V_{int} we use a simplified model potential (taken from [4]) that reproduces the characteristics of the exact e^-+H_2^+ coupling potential with sufficient accuracy. In this model the $\lambda_1(R)$ and $\lambda_2(R)$ functions from (1.9) are given by

$$\lambda_1(R) = \alpha_1 \left(1 - \tanh\left[\frac{\alpha_2 - R - \alpha_3 R^4}{7}\right]\right)\left(\tanh\left[\frac{R}{\alpha_4}\right]\right)^4, \tag{1.33}$$

$$\lambda_2(R) = \frac{1}{3}, \tag{1.34}$$

and the limit (1.11) then gives

$$V_{\text{int}}^{\infty}(r) = -2\alpha_1 \frac{e^{-r^2/3}}{r}. \tag{1.35}$$

The parameters are also listed in Table 1.1. Fig. 1.2 shows the shape of the full effective potential $V(R, r)$ in the interaction region.

For better visualisation and interpretation of the cross sections provided in the following chapter it is useful to calculate potential energy curves $V_n(R) = V_0(R) + E_n^{\text{el}}(R)$. Here $E_n^{\text{el}}(R)$ is the energy of an electron in the n-th Rydberg state at fixed internuclear distance R. It is an eigenvalue of a generalized version of the equation (1.23) satisfying

$$[H_0^{\text{el}} + V_{\text{int}}(R, r)]\rho_n(R, r) = E_n(R)\rho_n(R, r), \tag{1.36}$$

where R is a fixed parameter. We use these potential energy curves $V_n(R)$ to obtain vibrational energies corresponding to each Rydberg state which we then highlight in the calculated cross sections. The curves are shown in Fig. 1.3.

Parameter	Value/a.u.	Parameter	Value/a.u.
μ	918.076	α_1	1.6435
l	1	α_2	6.2
β_1	0.1027	α_3	0.0125
β_2	0.69	α_4	1.15
R_0	2.0		

Table 1.1: Values of parameters for the e^-+H_2^+ model (given in atomic units) that give potential energy in Hartrees

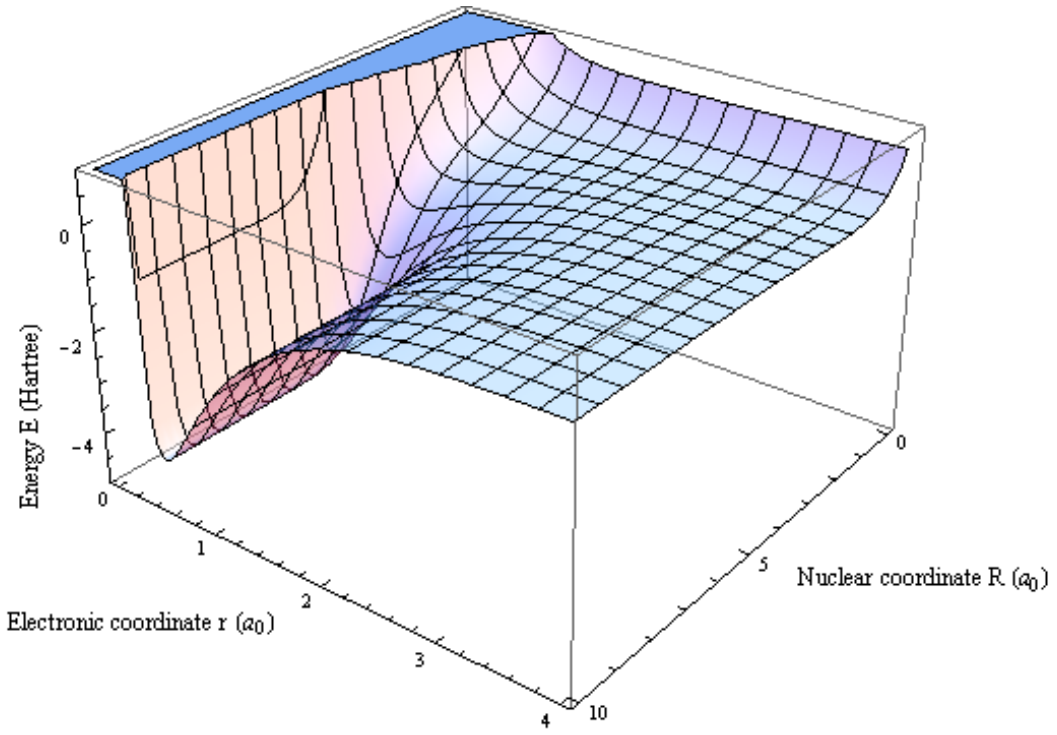

Figure 1.2: Effective potential (1.10) for the $e^- + H_2^+$ system in the interaction region.

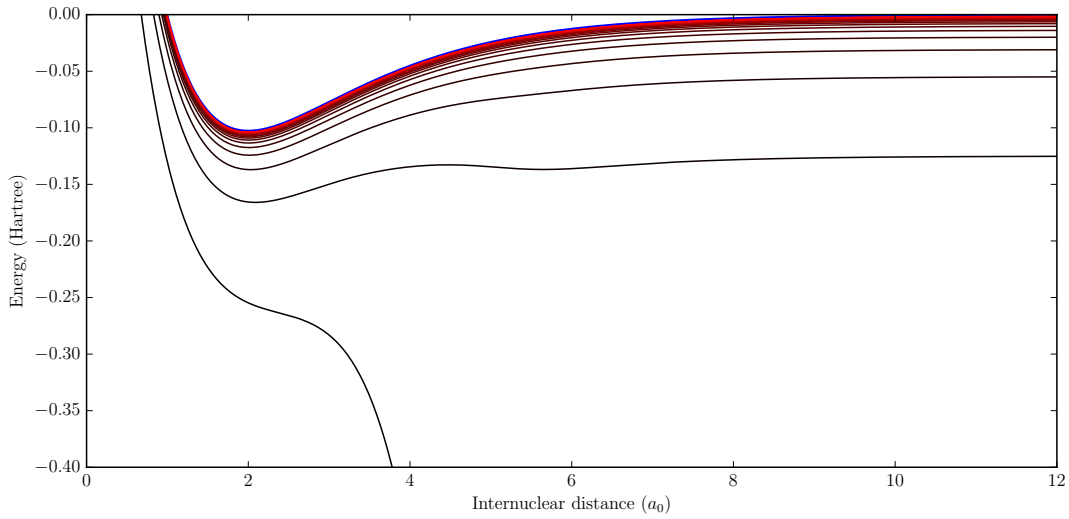

Figure 1.3: Potential energy curves obtained using fixed nuclei calculations. The blue curve is the cation potential $V_0(R)$ and the curves colored black to red are the $V_n(R)$ potentials.

1.3 Numerical methods

To represent continuous variables we use the finite element method with discrete variable representation (FEM-DVR) first proposed for solving quantum mechanical scattering problems by Rescigno and McCurdy [5]. We then combine this technique with exterior complex scaling (ECS) to simplify boundary conditions (more on that later). Our two-dimensional grid is obtained simply as a product

of two 1D grids of the nuclear and electronic variables.

1.3.1 Finite elements and discrete variable representation

The FEM discretization consists of dividing the assumed region of the continuous variable into multiple (N_{FE}) elements and upon each element the DVR method defines a basis function set (let their total number per element be n_q). Our basis consists of Lagrange interpolation polynomials through Gauss-Lobatto quadrature points $r_j^{(k)}$ (here k numbers the elements and j the quadrature points). Let $w_j^{(k)}$ denote the corresponding Gauss-Lobatto weights. The elements are connected by their first and last quadrature points satisfying $r_{n_q}^{(k)} = r_1^{(k+1)}$ (for $k = 1, ..., N_{FE} - 1$). We define the j-th Lagrange interpolation polynomial on the k-th element as

$$l_j^{(k)}(r) = \prod_{i=1, i\neq j}^{n_q} \frac{r - r_i^{(k)}}{r_j^{(k)} - r_i^{(k)}}, \tag{1.37}$$

which satisfies

$$l_j^{(k)}\left(r_i^{(k)}\right) = \delta_{ij}. \tag{1.38}$$

Let $f_j^{(k)}(r)$ denote the j-th basis function on the k-th element (not yet defined). We want them to be something along the lines of $l_j^{(k)}(r)/\sqrt{w_j^{(k)}}$ for r on the k-th element and zero outside. We will however add a few alterations due to the following conditions. They have to be zero at the edges of the grid to satisfy the Dirichlet condition so we leave out the very first and very last basis function. They also have to be continuous so we rescale and join the last and first basis functions of neighboring elements. Altogether we can define the basis functions in the following way

$$\text{for: } j = 2, ..., n_q - 1 \text{ and } k = 1, ..., N_{FE}$$

$$f_j^{(k)}(r) = \begin{cases} \frac{1}{\sqrt{w_j^{(k)}}} l_j^{(k)}(r), & \text{for } r_1^{(k)} \leq r \leq r_{n_q}^{(k)}, \\ 0, & \text{otherwise}, \end{cases} \tag{1.39}$$

$$\text{for: } j = n_q \text{ and } k = 1, ..., N_{FE} - 1$$

$$f_{n_q}^{(k)}(r) = \begin{cases} \frac{1}{\sqrt{w_{n_q}^{(k)} + w_1^{(k+1)}}} l_{n_q}^{(k)}(r), & \text{for } r_1^{(k)} \leq r \leq r_{n_q}^{(k)}, \\ \frac{1}{\sqrt{w_{n_q}^{(k)} + w_1^{(k+1)}}} l_1^{(k+1)}(r), & \text{for } r_1^{(k+1)} \leq r \leq r_{n_q}^{(k+1)}, \\ 0, & \text{otherwise}, \end{cases} \tag{1.40}$$

The total number of independent basis functions is then $n_b = N_{FE}(n_q - 1) - 1$. We can then mark the basis functions with a single index $I = 1, ..., n_b$ and arrange them by the order of the grid point in which they are non-zero (thanks to (1.38) each function has a single unique grid point where it is non-zero). There is a one-to-one correspondence between I and the pair (j, k) given by

$$\begin{aligned} I &= (k-1)(n_q) + (j-1), \\ j &= (I \mod n_q) + 1, \\ k &= (I \div n_q) + 1. \end{aligned} \tag{1.41}$$

We now write

$$f_I(r) = f_j^{(k)}(r), \tag{1.42}$$

$$r_I = r_j^{(k)}, \tag{1.43}$$

$$\begin{aligned} w_I &= w_j^{(k)}, && \text{for } j = 2, ..., n_q - 1, \\ w_I &= w_{n_q}^{(k)} + w_1^{(k+1)}, && \text{for } j = n_q. \end{aligned} \tag{1.44}$$

Thanks to (1.38) we can also write

$$f_I(r_J) = \frac{\delta_{IJ}}{\sqrt{w_I}}. \tag{1.45}$$

Since we chose our grid points to be Gauss-Lobatto quadrature points, we can approximate the integration of a function $F(r)$ over the grid region as

$$\int_{r_1}^{r_{n_b}} F(r)\mathrm{d}r \approx \sum_{I=1}^{n_b} F(r_I)w_I. \tag{1.46}$$

From this we get the effective orthogonality relation

$$\int_{r_1}^{r_{n_b}} f_I(r)f_J(r)\mathrm{d}r \approx \delta_{IJ}. \tag{1.47}$$

A function on the grid can be approximated by a linear combination of the basis functions

$$F(r) \approx \sum_{I=1}^{n_b} F_I f_I(r). \tag{1.48}$$

Using this, (1.47) and (1.46) we aquire the decomposition coefficients

$$F_I = F(r_I)\sqrt{w_I}. \tag{1.49}$$

Extending this into two dimensions is quite straightforward. Let's say we have an electronic grid with index $I = 1, ..., n_{b1}$ and a nuclear grid with index $J = 1, ..., n_{b2}$ with their corresponding grid points r_I and R_J, basis functions $f_I(r)$ and $g_J(R)$ and weights w_I and W_J respectively. We can combine the two indices into one $K = (J-1)n_{b1} + I$ and define combined coordinates x, basis functions h and weights ω

$$x_K = (r_I, R_J), \tag{1.50}$$

$$h_K(r, R) = f_I(r)g_J(R), \tag{1.51}$$

$$\omega_K = w_I W_J. \tag{1.52}$$

Also let $n_b = n_{b1}n_{b2}$. Analogically to (1.46) the integration of a function $F(r, R)$ over the entire region is approximated as

$$\int_{r_1}^{r_{n_{b1}}} \int_{R_1}^{R_{n_{b2}}} F(r, R)\mathrm{d}R\mathrm{d}r \approx \sum_{I=1,J=1}^{n_{b1},n_{b2}} F(r_I, R_J)w_I W_J = \sum_{K=1}^{n_b} F(x_K)\omega_K. \tag{1.53}$$

We then get more analogous forms

$$\int_{r_1}^{r_{n_{b1}}} \int_{R_1}^{R_{n_{b2}}} h_K(r, R)h_{K'}(r, R)\mathrm{d}R\mathrm{d}r = \delta_{KK'}, \tag{1.54}$$

$$F(r,R) \approx \sum_{I=1,J=1}^{n_{b1},n_{b2}} F_{I,J} f_I(r) g_J(R) = \sum_{K=1}^{n_b} F_K h_K(r,R), \tag{1.55}$$

$$F_K = F_{I,J} = F(r_I, R_J)\sqrt{w_I W_J} = F(x_K)\sqrt{\omega_K}. \tag{1.56}$$

In this notation we represent 2D wave functions with vectors of coefficients and quantum operators with matrices. The Schrödinger equation becomes a set of linear equations.

Thanks to our choice of DVR basis functions, potentials like V_{int}, V_0, the centrifugal and Coulombic term are represented by diagonal matrices (on the combined 2D index).

$$\begin{gathered} V_{KK'} = \langle h_K | \, V \, | h_{K'} \rangle = \int\int h_K^*(r,R) V(r,R) h_{K'}(r,R) \mathrm{d}r \mathrm{d}R \approx \\ \textstyle\sum_{L=1}^{n_b} \omega_L h_K^*(x_L) V(x_L) h_{K'}(x_L) = V(x_K)\delta_{KK'}. \end{gathered} \tag{1.57}$$

Additionally, the kinetic terms become very sparse matrices. This means that the entire Hamiltonian is represented by a sparse matrix and solving the corresponding Schrödinger equation becomes numerically easy. Furthermore, volume integrals like (1.25) and (1.26) become simple. Let

$$\begin{aligned} \phi(r,R) &= \textstyle\sum_{K=1}^{n_b} \phi_K h_K(r,R), \\ \psi(r,R) &= \textstyle\sum_{K'=1}^{n_b} \psi_{K'} h_{K'}(r,R). \end{aligned} \tag{1.58}$$

Then

$$\begin{gathered} \langle \phi | \, V \, | \psi \rangle = \textstyle\sum_{K=1,K'=1}^{n_b,n_b} \phi_K^* \psi_{K'} \langle h_K | \, V \, | h_{K'} \rangle \approx \\ \textstyle\sum_{K=1,K'=1}^{n_b,n_b} \phi_K^* \psi_{K'} \delta_{KK'} V(x_K) = \sum_{K=1}^{n_b} \phi_K^* \psi_K V(x_K). \end{gathered} \tag{1.59}$$

1.3.2 Exterior complex scaling

The third method, exterior complex scaling (described in depth in [6]), consists of bending the coordinate into the complex plane at a certain point R_0 far from the interaction region

$$r'(r) = \begin{cases} r, & r < R_0, \\ R_0 + (r - R_0)e^{i\theta}, & r \geq R_0. \end{cases} \tag{1.60}$$

When combining ECS with FEM we have to make sure to choose the bending point R_0 coincident with one of the finite element nodes r_i. Additionally we have to adjust the Gauss-Lobatto weights for the complex grid points that come after the bending point. For most we merely multiply them by $e^{i\theta}$. For the bending point

$$w_I = w_{n_q}^{(k_{bend})} + w_1^{(k_{bend}+1)} \to w_I^{ECS} = w_{n_q}^{(k_{bend})} + w_1^{(k_{bend}+1)} e^{i\theta}. \tag{1.61}$$

When using the ECS method we have to watch out for potentially non-trivial changes to Hamiltonian behaviour caused by adding a complex part to the coordinate. In our case, the interaction potential (1.9) contains the term $\tanh\left[(\alpha_2 - R - \alpha_3 R^4)/7\right]$. The hyperbolic tangent function does not cause any problems for real arguments and behaves well for most complex arguments. But

along a trajectory with a near zero real part and a quickly changing imaginary part it will explode (can be seen in Fig. 1.4) making numerical evaluation unstable. The argument $(\alpha_2 - R - \alpha_3 R^4)/7$ contains the term R^4. Its real part changes its sign for ECS with an angle of more than $\pi/8$. So for angles over $\pi/8$ there will exist a point on the complex part of the grid (given it is long enough), where the real part of $(\alpha_2 - R - \alpha_3 R^4)/7$ passes through zero. At the same time the imaginary part is a quickly changing value. This will likely result in extremely erratic behaviour of the potential in a small area around this point, which could potentially cause problems for our numerical calculation on a discretized grid. The point where $Re[(\alpha_2 - R - \alpha_3 R^4)/7]$ passes zero moves into infinity with angles approaching $\pi/8$ - shown in Fig. 1.5. Therefore the bending angle must be less than $\pi/8$.

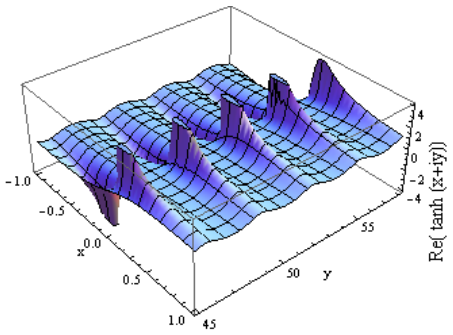

(a) Real part of Tanh

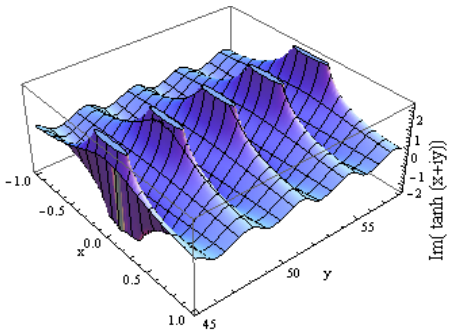

(b) Imaginary part of Tanh

Figure 1.4: Behaviour of hyperbolic tangent on complex plane for arguments with real part around zero.

Finally, the channel Hamiltonian may contain non-negligible potential at the bending point. As long as it is repulsive, there is no possibility of reflection from it beyond the bending point. However, our electronic channel Hamiltonian contains a Coulomb term which is attractive and non-vanishing. This issue only affects the bound states that have non-negligible amplitude beyond the bending point. So our solution will approximate the real solution well if the solution's overlap with problematic states is negligible. Therefore we must choose the bending point far enough for the computation to be stable.

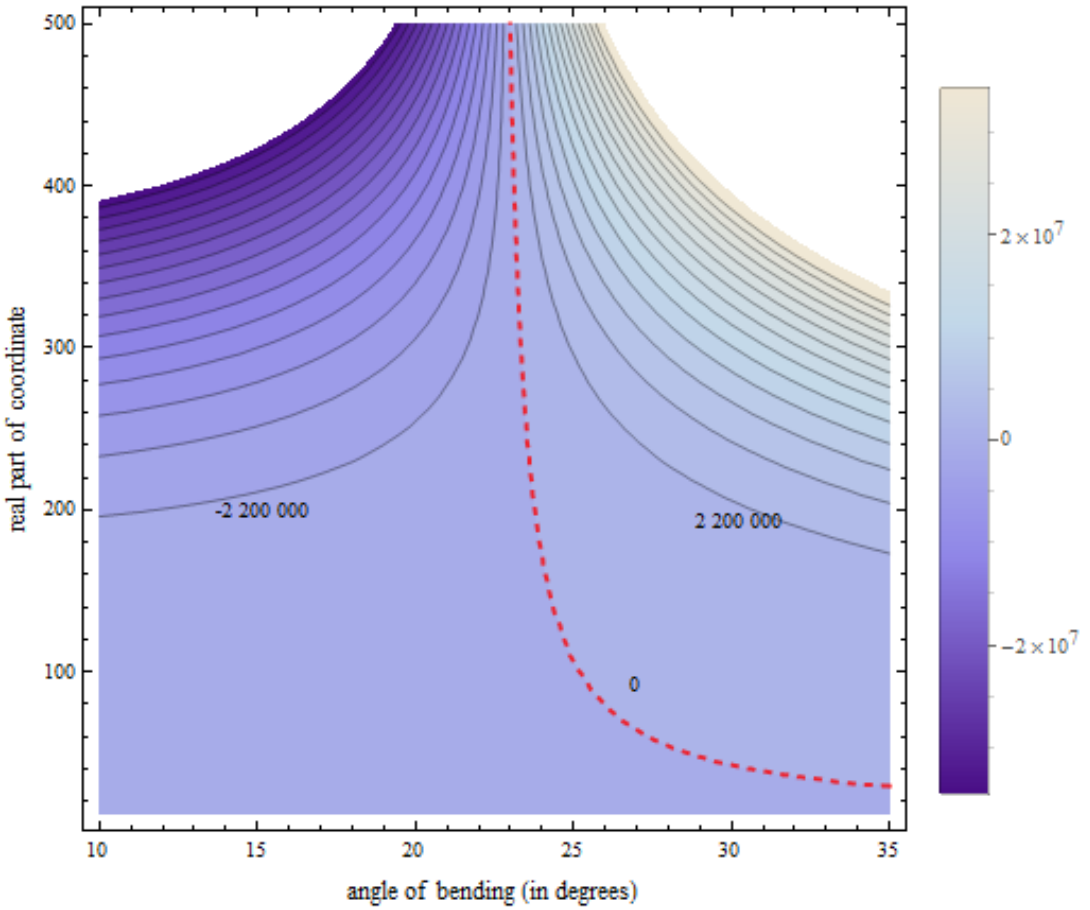

Figure 1.5: A contour plot of $Re[(\alpha_2 - R - \alpha_3 R^4)/7]$ showing how on an ECS grid, for a bending angle decrasing towards $\pi/8$, the "point of passing zero" (red dashed line) goes into infinity. The point of bending is set equal to 12 (changing it slightly alters the contour lines but not in a significant way). Some of the contour lines are marked.

1.3.3 Solution of the Schrödinger equation

Instead of solving the Lippmann-Schwinger equation we actually solve the driven Schrödinger equation (obtained by combining (1.13), (1.14) and (1.15))

$$(E - H)\,|\psi_{sc}\rangle = V_{\text{int}}\,|\psi_{in}\rangle\,. \tag{1.62}$$

This is the actual equation that we solve (for an unknown ψ_{sc}) in our numerical computation. Doing this on an ECS grid effectively makes it equivalent to solving the Lippmann-Schwinger equation and inverting the complex scaled term $(E-H)$ is equivalent to finding $G^+(E)$.

Under the ECS transformation, any function behaving like a pure outgoing wave at large distances, e.g.

$$F(r) \underset{r\to\infty}{\sim} Ce^{ikr}, \text{ with } k > 0, \tag{1.63}$$

will decrease exponentially with r approaching infinity.

$$F(r^{ECS}(r)) \underset{r\to\infty}{\sim} Ce^{ikre^{i\theta}} = Ce^{ikr\cos\theta - kr\sin\theta} \to 0, \text{ for } 0 < \theta < \pi, \tag{1.64}$$

Hence we get to the main reason for employing ECS: by using it we avoid the need to explicitly impose asymptotic boundary conditions in both vibrational excitation (an outgoing electron) and dissociative recombination (an outgoing atom). Because of this we use ECS for both the electronic and nuclear coordinate.

2. Results

In all of our calculations we used an initial state with the lowest (zeroth) molecular vibrational state so v_i is always zero. Thus in the whole chapter we use a simplified notation to symbolize the channels

$$\mathrm{DR}(v_i = 0 \to n) = \mathrm{DR}_n,$$
$$\mathrm{VE}(v_i = 0 \to v_f) = \mathrm{VE}_{v_f},$$

where n denotes the final Rydberg state.

2.1 Cross sections

Firstly, let us look at the calculated cross sections for the whole range of energies from 0 to 0.05 Hartrees where three dissociative recombination and five vibrational excitation (plus elastic scattering) channels are open. We start with these broad pictures to give the reader a better understanding of how the cross sections behave and which regions of energy might be problematic and how.

All of these calculations were done on a grid on which we settled after extensive tests of convergence which we will cover in the next subchapter. The parametrization of this final grid is in Table 2.1.

Electronic coordinate parametrization, $n_q = 6, \theta = 20°$							
real part							
Endpoints	1	4	20	100	1300	-	
Elements	8	12	8	16	120	-	
complex scaled part							
Endpoints	1350	1400	1500	1700	2000	3000	100000
Elements	5	2	1	1	1	1	5
Nuclear coordinate parametrization, $n_q = 6, \theta = 20°$							
real part							
Endpoints	1	3	4	12	-		
Elements	12	24	12	120	-		
complex scaled part							
Endpoints	12.5	14	18	58	200	1000	10000
Elements	8	6	2	4	3	3	3

Table 2.1: The parameters of our final FEM-DVR-ECS grids. Both grids start at 0. The number of elements under each endpoint is the number of elements on the interval between the previous endpoint and this one (the first real part interval starts at 0). n_q is the quadrature order and θ the bending angle.

The DR and VE cross sections of all the open channels are shown in Fig. 2.1 and Fig. 2.2 respectively. In the DR graphs we also highlighted the vibrational thresholds and all the graphs contain light pink highlighted regions just below these thresholds. Looking at the graphs, we can see that within these regions peaks become more and more densely packed as they approach the vibrational threshold but then they stop and the curve becomes flat before reaching the

threshold. Ideally there would be an infinite amount of peaks just below the threshold. This is caused by the fact that there is actually an infinite number of Rydberg states but a finite grid only provides a finite amount. So when calculating the cross sections there will always exist regions of energy just below the vibrational excitation thresholds where the calculated values are not converged. Enhancing the grid makes these regions smaller (adds more peaks) but they never completely disappear. The pink regions are extended to also contain several of the peaks since their values are also not converged. Outside these regions the cross sections are converged.

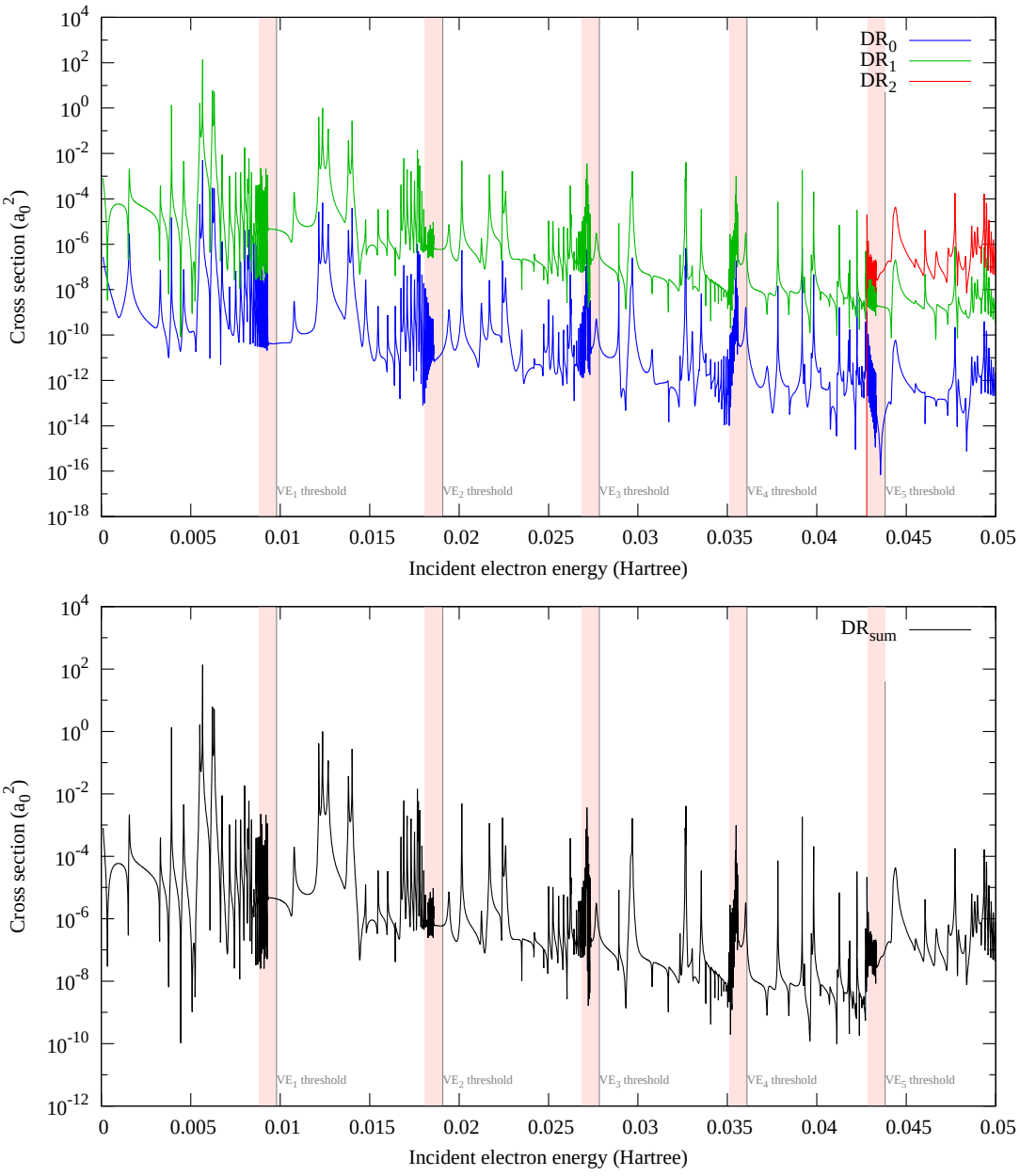

Figure 2.1: The dissociative recombination cross sections of the first three channels. The light pink regions show where the calculated values are inaccurate.

Fig. 2.1 also contains the sum of all DR cross sections. We see that for the most part the cross sections differ by several orders and the sum merely corresponds to the dominant channel for a given energy. Most notably, the channel

DR_0 has a far smaller cross section for all energies and thus its contribution to the sum is completely negligible.

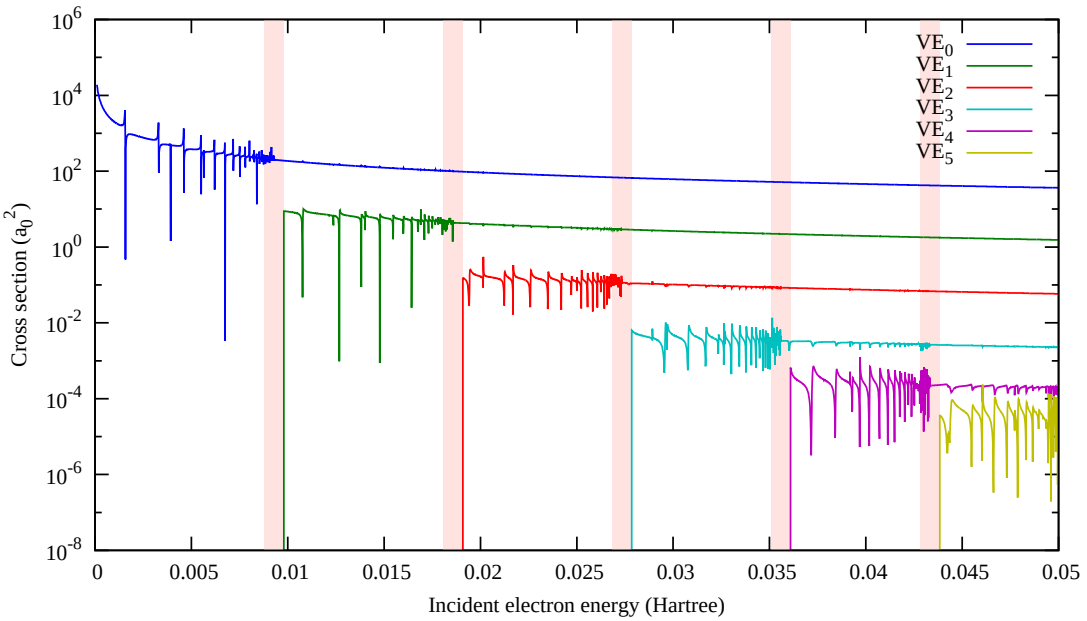

Figure 2.2: The elastic scattering (VE_0) and vibrational excitation cross sections. The light pink regions show where the calculated values are inaccurate.

2.2 Tests of convergence

There are two key aspects that we test for our 2D FEM-DVR-ECS grid:

- Density - it needs to be high enough to give accurate results but also not too high as to cause the calculation to be time consuming. It is determined by the order of the quadrature and the density of finite elements. Important for both the electronic and the nuclear grid.

- Position of the ECS bending point - placing it further out makes the calculation more accurate but forces us to set additional finite elements to keep the density constant. The nuclear variable potentials are quickly vanishing, so we only need to place the nuclear grid bending point far enough for them to be negligible beyond it. The electronic variable is more problematic because of the long range Coulombic potential. Extending it further always gives more Rydberg states.

The parametrization of the final grid that we used for the final cross section calculations is in the previous subchapter (Table 2.1). The graphs in Fig. 2.3, Fig. 2.4 and Fig. 2.5 all show energy ranges just below the three highest (in the studied range of energies $\langle 0; 0.05 \rangle$) vibrational excitation thresholds since the cross section values in these ranges change the most when altering the grid.

As we can see from Fig. 2.3, where dependence of results on the chosen bending point R_0 is shown for the VE_1 cross section, the results are well converged

for most energies and are untrustworthy only for a small range of values below the vibrational excitation thresholds.

Fig. 2.4, showing the dependence of results on the chosen electronic grid quadrature for the DR_1 channel, shows that results for our chosen grid are well converged for all energies except for the problematic regions determined by the ECS bending point. However, we see that at higher energies the lower density grid starts diverging. So if we were to significantly extend our energy range, we would need to increase the grid density.

Fig. 2.5 shows similar results for changing the nuclear grid density. For these densities a difference was only visible in the DR_0 channel where the values are lowest and thus the value discrepancy is most apparent.

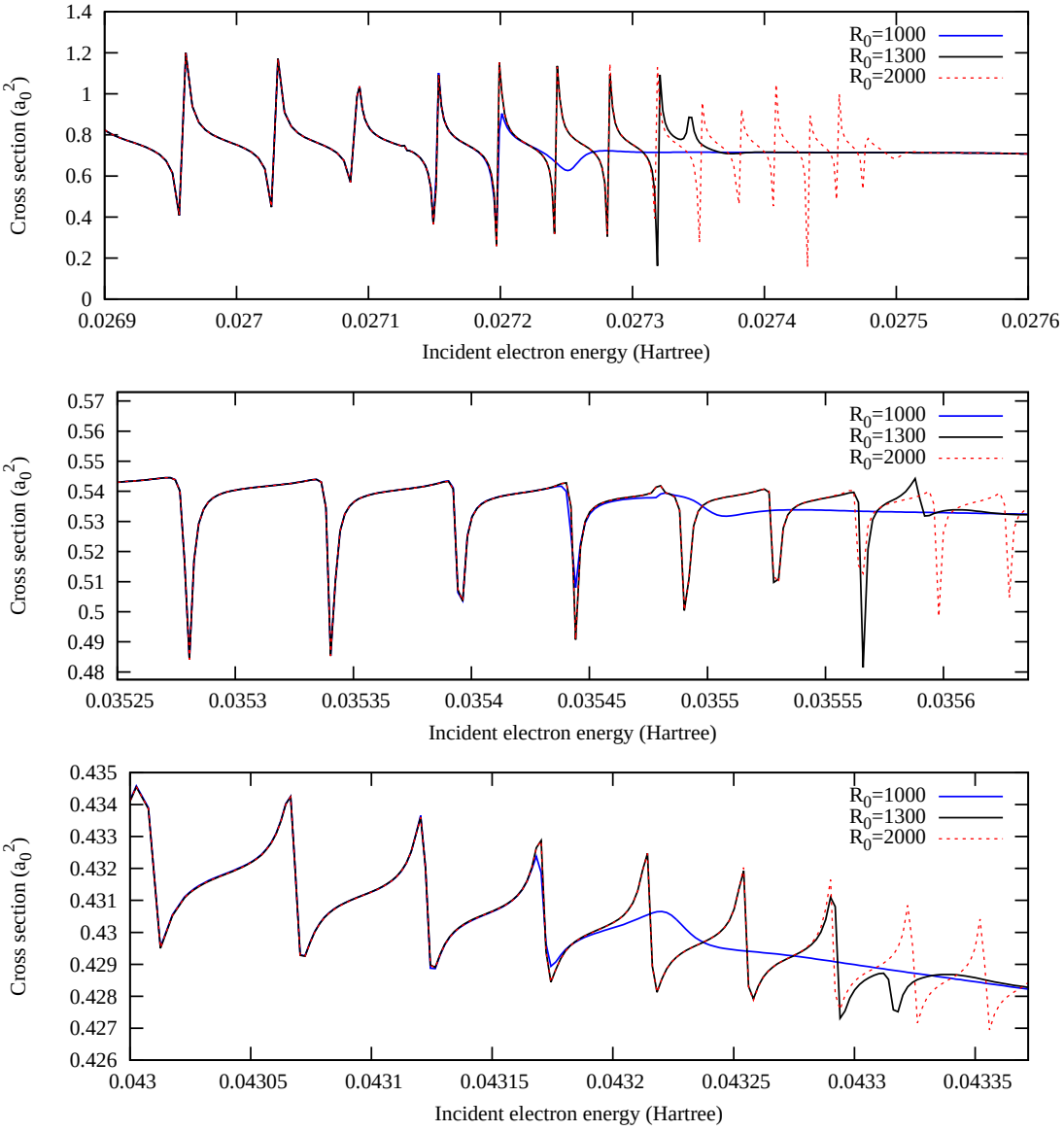

Figure 2.3: A comparison of calculated cross sections for the VE_1 channel for three electronic grid bending point positions R_0. The energy ranges are chosen close to the three highest vibrational excitation thresholds which are at energies approximately 0.0278, 0.0361 and 0.0438 Hartree. The black curve represents the results for the grid we use in our main calculations.

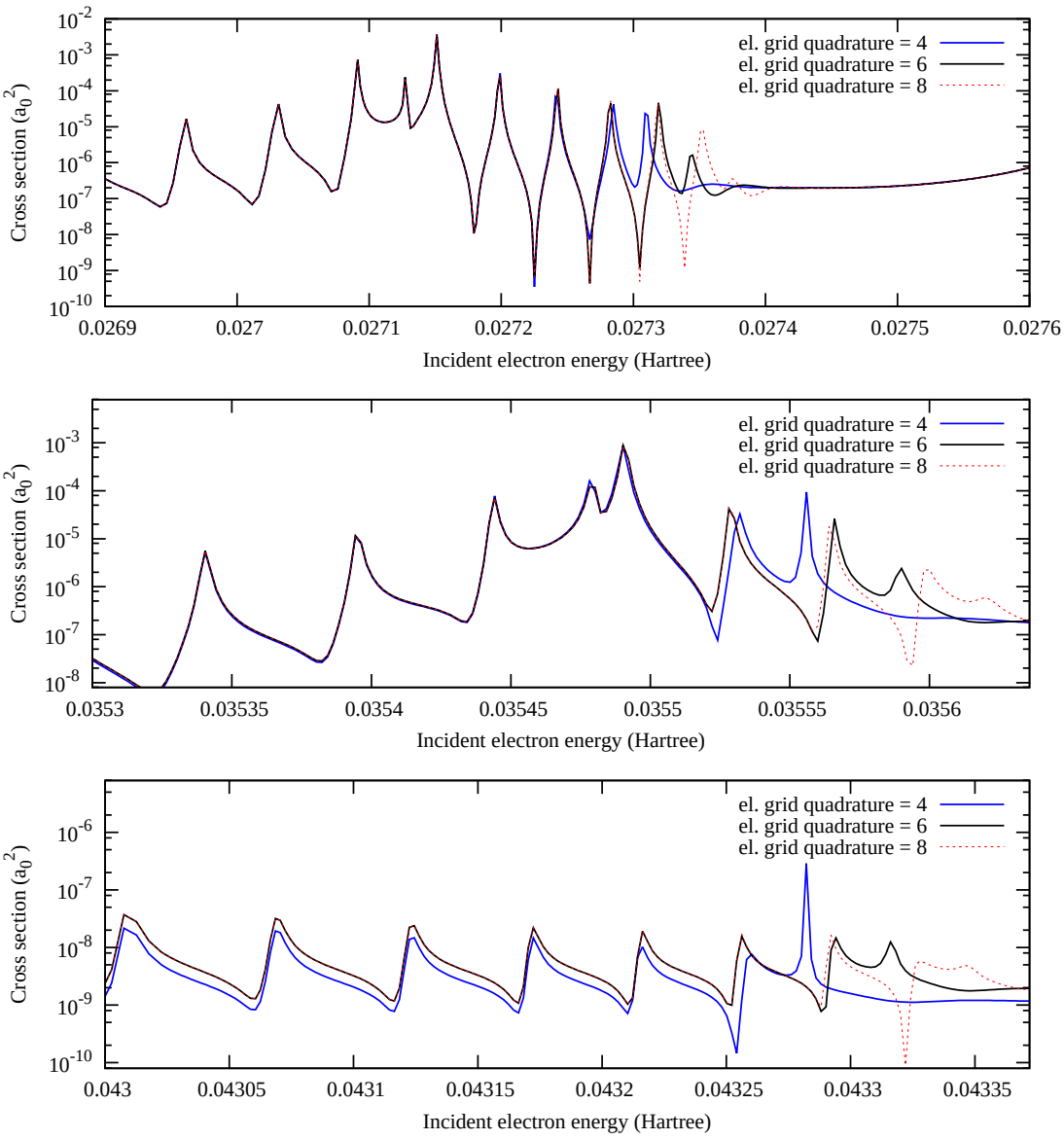

Figure 2.4: A comparison of calculated cross sections for the DR_1 channel with varying electronic grid quadrature order (while the number of elements was kept fixed). Again we choose to show energy ranges close to the thresholds and the black curve represents our chosen grid.

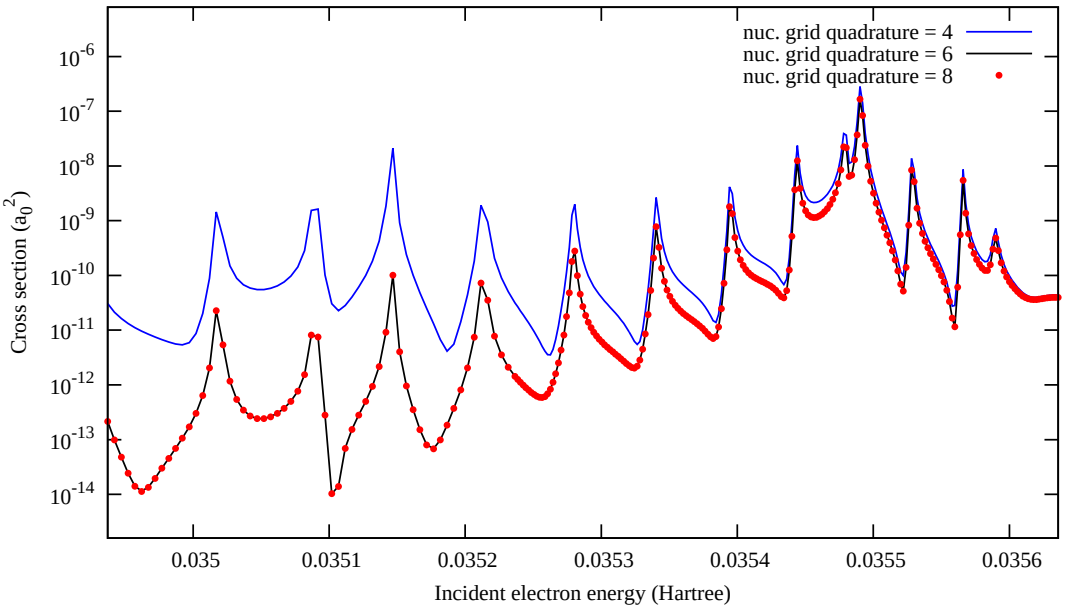

Figure 2.5: A comparison of calculated cross sections for the DR_0 channel with varying nuclear grid quadrature order (while the number of elements was kept fixed). The black curve represents our chosen grid. The higher density grid results are plotted with points since they match the black line perfectly.

We also tested changing the finite element densities and shifting the nuclear grid bending point (and we always tested all the channels) but those results do not show anything qualitatively different from the behaviour described above, therefore we omitted them.

2.3 Interpretation of structures in the cross sections

To better understand the structures in the cross sections we have to look back at Fig. 1.3 showing the potential energy curves $V_n(R) = V_0(R) + E_n^{\mathrm{el}}(R)$. We can use them to get the vibrational energies and vibrational thresholds corresponding to the Rydberg states. Fig. 2.6 shows the potential energy curves in more detail with highlighted vibrational levels.

We see from Fig. 1.3 that the first two channels (DR_0 and DR_1) are open for all incident electron energies. We also note that the ground state potential (channel DR_0) rapidly drops into very low energies and asymptotically goes below -1.4 Hartree. This state does not correspond to any physical state of the $e^-+H_2^+$ system and is an artefact of the model interaction potential. This does not need to concern us since its cross section is completely negligible (as shown in the first subchapter).

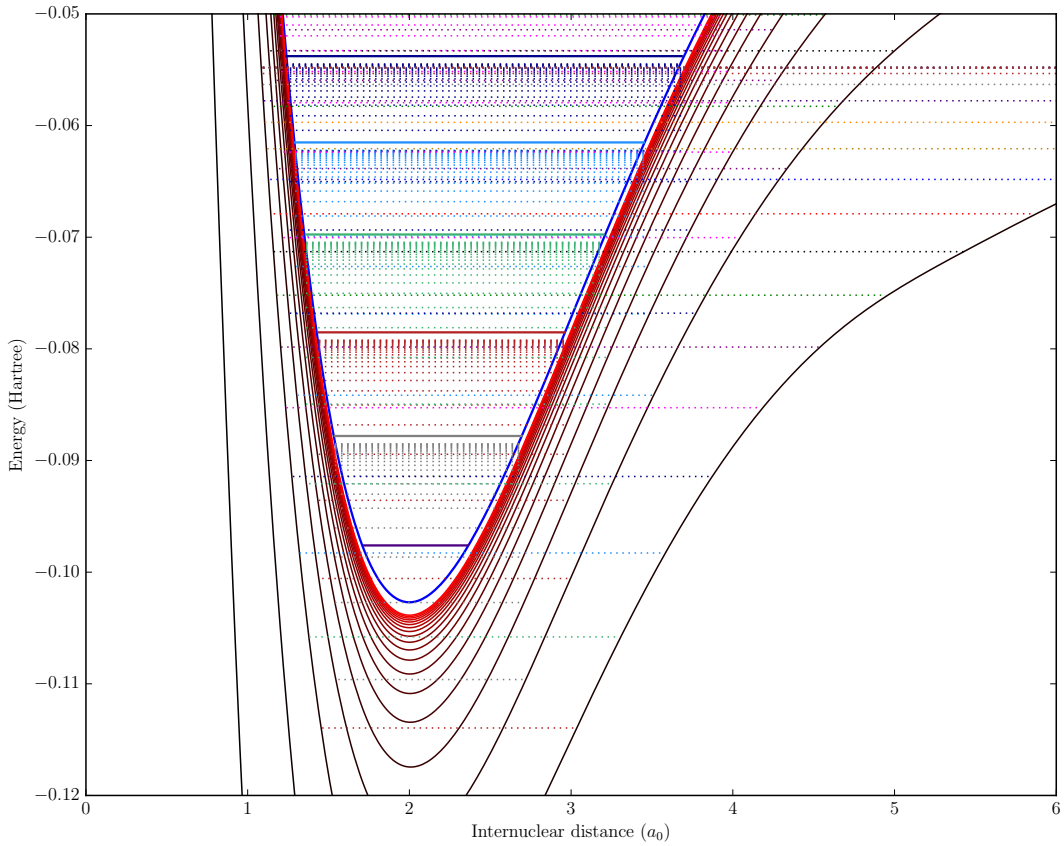

Figure 2.6: A zoomed in picture of the potential energy curves. The added lines represent vibrational energies. Each vibrational level is represented by a distinct color. Different lines of the same color stand for the same vibrational level in different Rydberg states. The solid and dashed lines correspond to vibrational levels in the cation potential $V_0(R)$ and vibrational levels in the Rydberg state potentials respectively. The zeroth vibrational level series is not included since it is inconsequential to the cross sections.

The following figures 2.7, 2.8, 2.9, 2.10, 2.11 and 2.12 show more detailed graphs of the cross sections in which we highlight the vibrational levels of several Rydberg states. They are highlighted with dashed vertical lines matching in color those in Fig. 2.6 and the vibrational thresholds are solid vertical lines also matching those in Fig. 2.6. The i-th level in the n-th Rydberg state is labeled ν_i^n. The pink regions are the same as in Fig. 2.1 and Fig. 2.2.

For better clarity we did not include the vibrational levels of all the calculated Rydberg states. We omitted the vibrational levels of the highest Rydberg states since they are very close to the vibrational thresholds. Including them would only add more densely placed lines close below the vibrational thresholds.

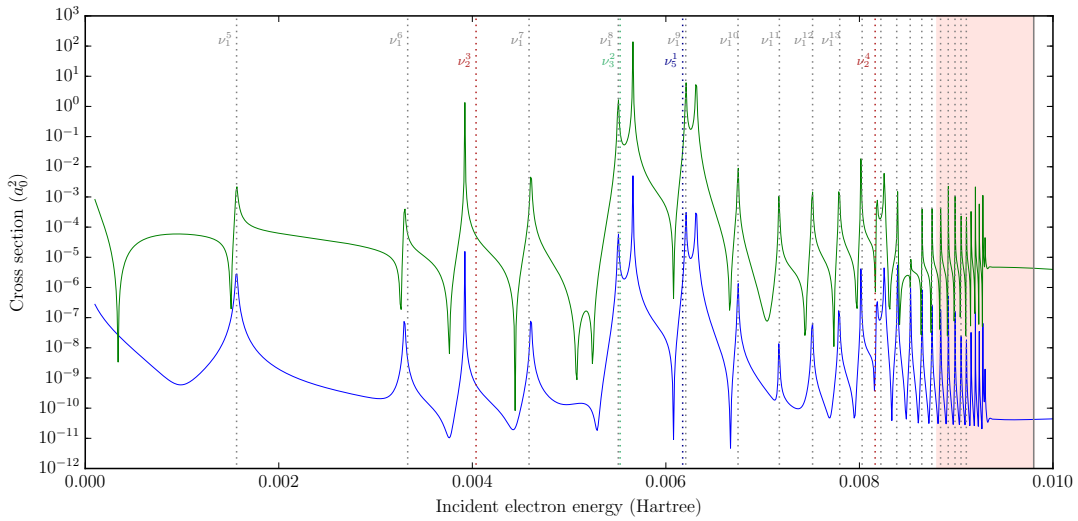

Figure 2.7: A detail of the lower energy dissociative recombination cross sections. The dashed lines represent energies of vibrational levels in Rydberg states. Their colors are the same as in Fig. 2.6. ν_i^n is the i-th level in the n-th Rydberg state. The curve colors are the same as in Fig. 2.1.

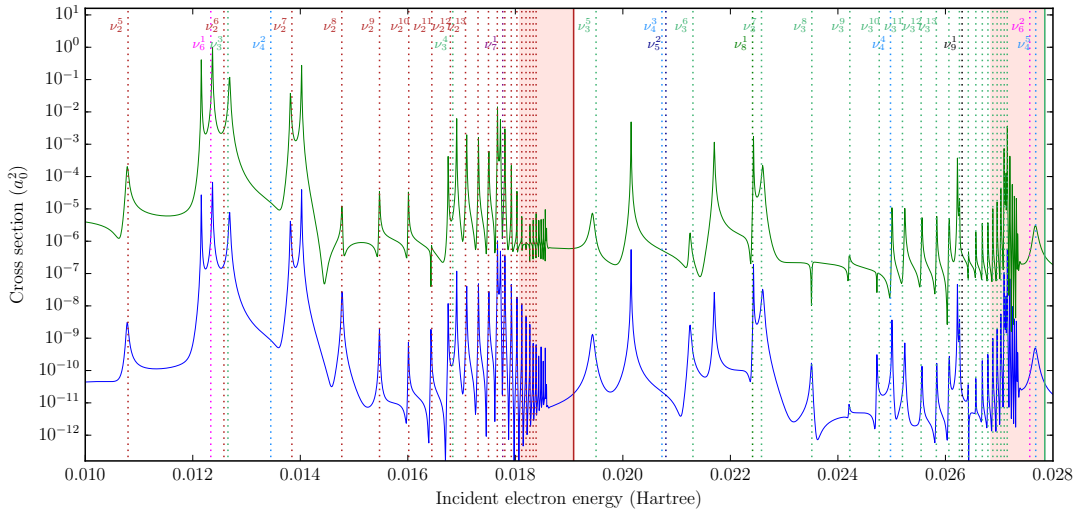

Figure 2.8: A continuation of Fig. 2.7 for higher energies.

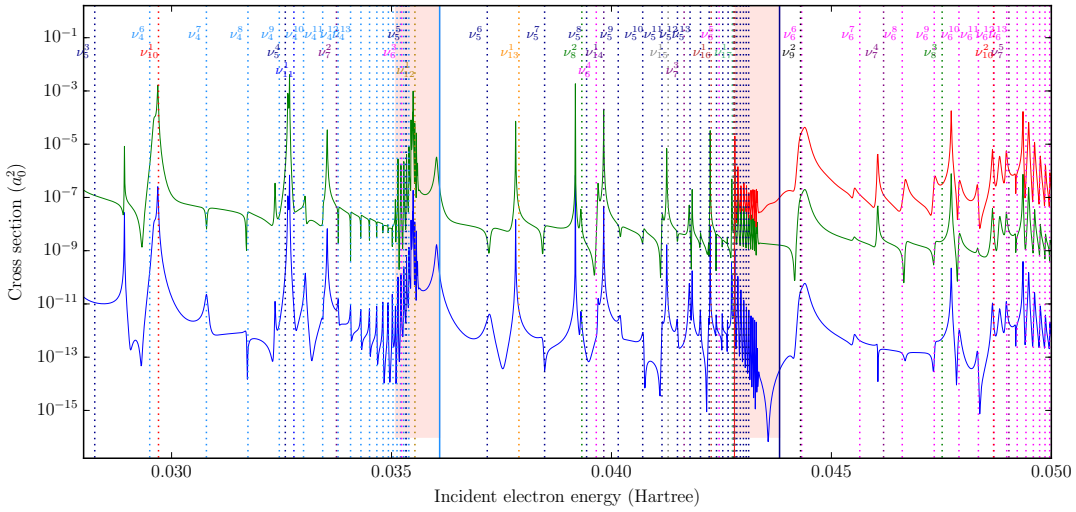

Figure 2.9: A continuation of Fig. 2.8 for the highest calculated energies.

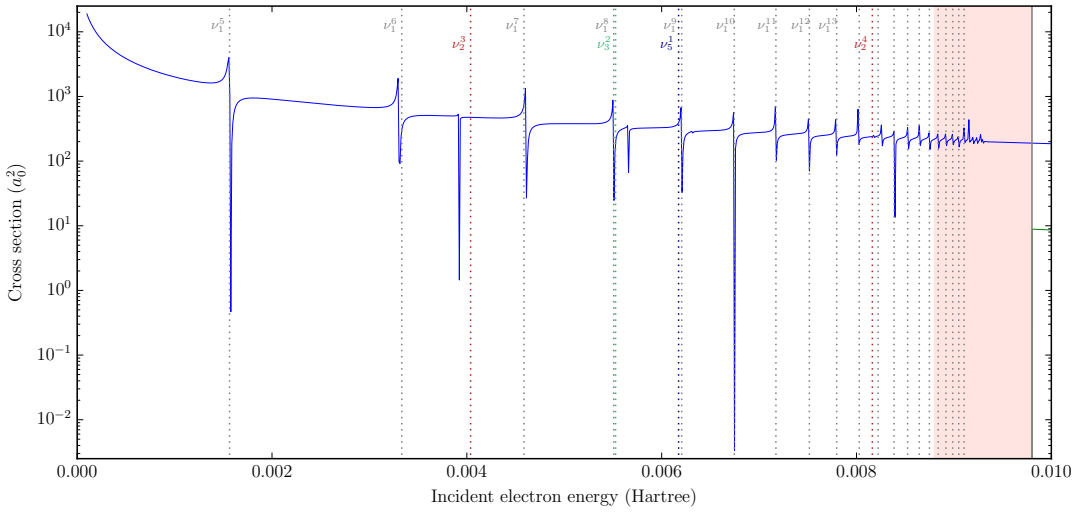

Figure 2.10: A detail of the lower energy vibrational excitation cross sections. The dashed lines represent energies of vibrational levels in Rydberg states. Their colors are the same as in Fig. 2.6. ν_i^n is the i-th level in the n-th Rydberg state. The curve colors are the same as in Fig. 2.2.

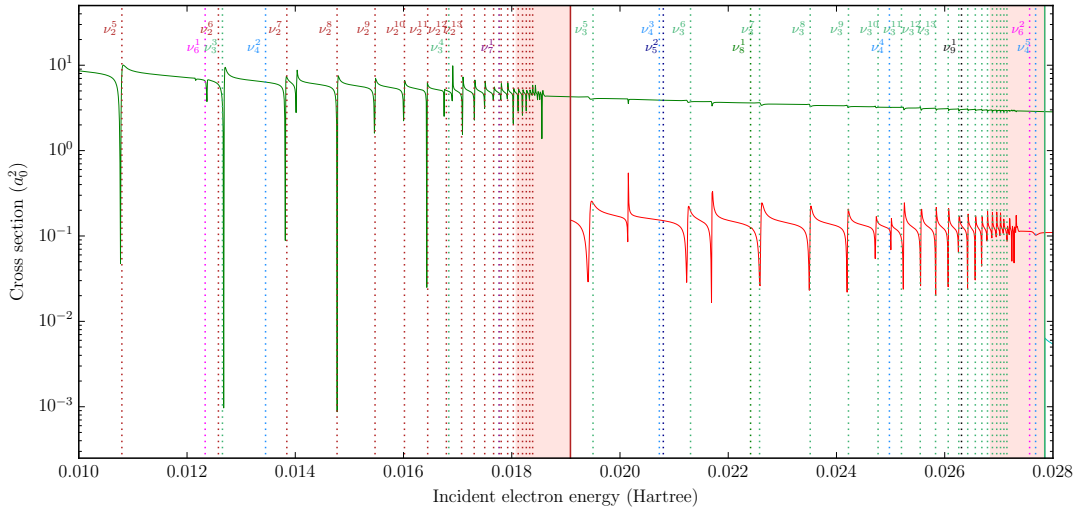

Figure 2.11: A continuation of Fig. 2.10 for higher energies.

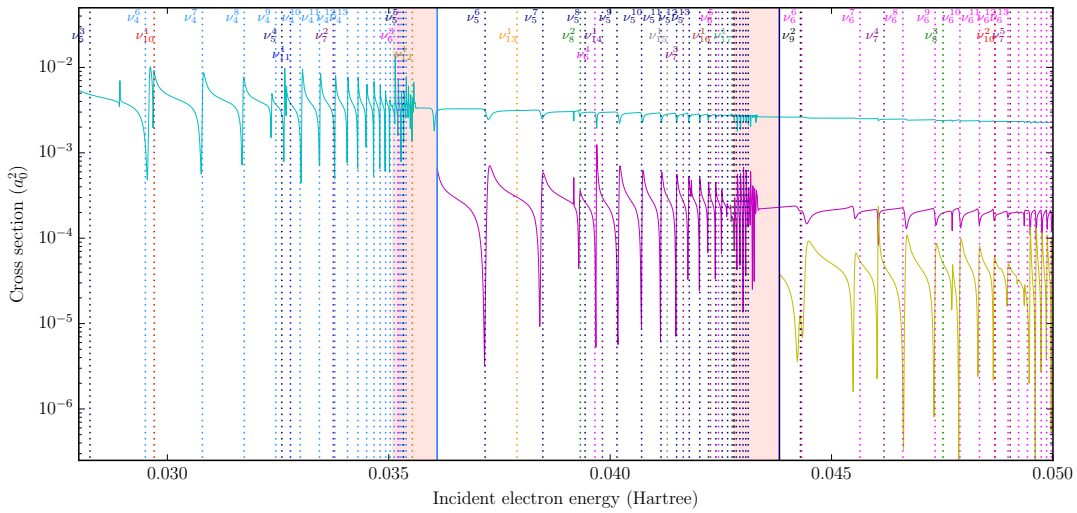

Figure 2.12: A continuation of Fig. 2.11 for the highest calculated energies.

Looking at the detailed figures we can see that most of the dashed lines sit quite precisely at peaks of the calculated cross sections. As the index of the vibrational level increases they start to be less coincident. This is most apparent for high vibrational levels of the lowest Rydberg states. Looking back at Fig. 1.3 we can see that the potential curves of the higher Rydberg states strongly resemble the cation potential $V_0(R)$ curve. This means that the interaction here is weak and there is much less room for complicated behaviour than for the low Rydberg states. Stronger interactions have a higher possibility of large level shifts.

We can also see many different peak shapes and structures probably resulting from interference like the double peaks around ν_1^8 and ν_3^2 or ν_5^1 and ν_1^9 in Fig. 2.7. Although most peaks are coincident with or close to vibrational level energy there are some that are quite far off from any dashed line, like for example the peak around 0.02015 Hartrees in Fig. 2.8.

Even more interesting is the peak at 0.00034 Hartrees in Fig. 2.7 because it is only present in the DR_1 channel and absent from both DR_0 and VE_0. We think that it is either a part of a larger structure corresponding to a certain vibrational level ν_i^n below the elastic scattering threshold. It could also be caused by the Ramsauer-Townsend effect.

We will be analyzing these structures more closely in the future once we start comparing our results with approximative methods.

Conclusion

We have successfully created a numerically solvable two-dimensional model of the indirect mechanism of dissociative recombination and vibrational excitation of diatomic molecular ions by electron impact. We solve this problem in the time independent picture. We have implemented the FEM-DVR-ECS method to numerically solve the problem for the case of a H_2^+ diatomic and calculated the DR and VE cross sections for a range of incoming electron energies from 0 to 0.05 Hartrees.

In the future we will compare these results with the results from commonly used approximative methods (such as the local complex potential approximation or the frame transformation theory based on quantum defect theory) to test their accuracy. We then plan to broaden the model into a two channel 2D model for both the direct and indirect DR mechanism.This extended model will further allow us to assess the accuracy of approximate methods.

Bibliography

[1] A. E. Orel M. Larsson. *Dissociative Recombination of Molecular Ions*. Cambridge University Press, Cambridge, 2008.

[2] A. Giusti. A multichannel quantum defect approach to dissociative recombination. *J. Phys. B*, 13(3867-3894), 1980.

[3] J.B.A. Mitchell A.I. Florescu-Mitchell. Dissociative recombination. *Physics Reports*, 430:277–374, 2006.

[4] E.L. Hamilton. Photoionization, photodissociation, and long-range bond formation in molecular rydberg states, 2003.

[5] T.W. Rescigno and C.W. McCurdy. Numerical grid methods for quantum-mechanical scattering problems. *Phys. Rev. A*, 62(032706), 2000.

[6] M. Baertschy C.W. McCurdy and T.W. Rescigno. Solving the three-body coulomb breakup problem using exterior complex scaling. *J. Phys. B*, 37(17), 2004.

List of Figures

List of Tables

List of Abbreviations

DR	dissociative recombination
DVR	discrete variable representation
ECS	exterior complex scaling
FEM	finite elements method
VE	vibrational excitation